

Annular acoustic impedance metasurfaces for encrypted information storage

Yu-Ze Tian,¹ Xiao-Lei Tang,¹ Yan-Feng Wang,^{1,*} Vincent Laude,² and Yue-Sheng Wang^{1,3}

¹*School of Mechanical Engineering, Tianjin University, 300350 Tianjin, China*

²*Université de Franche-Comté, CNRS, Institut FEMTO-ST, F-25000 Besançon, France*

³*Institute of Engineering Mechanics, Beijing Jiaotong University, Beijing 100044, China*

Extensive research has been devoted recently to the design of metasurfaces. Design strategies based on impedance theory stand out for power flow regulation. The designed impedance matrix is characteristic of a given pair of incident and modulated wave fields, hence providing opportunities for encrypted information storage. We consider acoustic vortices propagating along cylindrical shell waveguide as signal carriers. Within the shell waveguide, an annular acoustic impedance metasurface is introduced for encrypted information storage. Information stored in the metasurface would only be retrieved when interrogated with the correct input. Hidden messages are successfully read in numerical simulation when the three-layer model is used to implement the metasurface. A realistic structure based on Helmholtz resonant unit cells is further designed to verify experimentally the encryption storage process. This work is expected to spur more applications of impedance metasurface to acoustic holography and encrypted acoustic communications.

Keywords: Impedance metasurfaces; Acoustic metasurfaces; Information storage; Acoustic vortices

I. INTRODUCTION

Metamaterials have attracted great attention owing to their extensive functionality¹. Various novel applications have been reported and implemented during the last decade, including wave regulation²⁻⁵, heat flow management⁶, invisibility cloaking^{7,8}, holographic imaging⁹ and non-destructive evaluation^{10,11}. Information processing based on metamaterials¹²⁻¹⁴ is currently emerging, accompanied with a rising demand on minimization, integration, and increased information capacity. Metasurface, as a branch of metamaterial, appears to be a brilliant candidate in this respect¹⁵. It owns an extraordinary capability to compactly process information within a 2D artificial structure and can be integrated with multiple functions. Some achievements have been reported recently, including cross medium communication^{16,17}, oriented transmission¹⁸⁻²⁰, and acoustic vortex generation²¹ and decoding^{22,23}. However, the current designs sometimes suffer from an unsatisfactory transmission efficiency²⁴. The applicable scenarios are also very limited and reliability is a global concern.

A perfect solution for the power flow control of electromagnetic waves was originally given by Asatchy et al.²⁵ and is attracting extensive attention. In this setting, the metasurface together with the whole space surrounding it are regarded as a complete system. Wave propagation is described in terms of a characteristic interface impedance that can be precisely controlled without introducing parasitic scattering. By analogy, Díaz-Rubio et al. proposed a comprehensive discussion for refraction and reflection of acoustic waves²⁴. Reflective metasurfaces with perfect control on power flow were designed and verified numerically by the three-layer model. It was proven that the efficiency of the designed metasurfaces surpasses the theoretical limit for the generalized Snell's law. Li et al. then developed a quadruple Helmholtz resonator structure for practical construction of refractive

impedance metasurfaces²⁶. The unit can be designed independently and used to approach the impedance characteristics of the interface when its tangential dimension is deeply sub-wavelength. Metasurfaces obtained by describing wave field regulation via an impedance matrix are currently termed impedance metasurfaces.

Despite those promising prospects, there are some underlying limitations that cannot be ignored. Power flow on both sides needs to be strictly local in order for the metasurface to be discretized into independently designed units. Ideas for improvement were proposed, including the power flow-conformal design methodology²⁷⁻²⁹ and the in-plane transverse connection^{30,31}. These strategies, however, sometimes make the design more complex without extending the range of realizable functions that can be implemented. The balance of power flow is much more complicated in practice as well, especially when Gaussian beams rather than theoretical plane waves are used for excitation. In addition, unlike metasurfaces based on the generalized Snell's law, that provide a certain steering angle for any incident angle³², the impedance metasurface only works under a fixed incidence and transmission setting²⁴. Once fabricated, perfect output can only be observed under preset input. Interestingly, this feature allows the impedance metasurface to serve as a cipher lock, so that tailored information can only be correctly revealed in the output under specific inputs. Hence, it seems tempting to use it for the storage of encrypted information. So far, similar applications have been reported for optical³³ and mechanical metamaterials^{34,35}, but seldom for pressure acoustics.

In this paper, we design an annular acoustic impedance metasurface as an information processing device for encrypted information storage, with the idea that it might be a generic application turning the limitations of impedance theory into advantages. Cylindrical shell waveguides, supporting a controlled number of acoustic vortices and containing annular metasurfaces, are consid-

ered for implementation. Besides, the composition of the concentric annular waveguides enables more contents to be integrated in a limited footprint. Customized information is hidden inside the miniaturized annular structure in terms of acoustic vortices. Eight cases including five cases with a single output and three cases with a double output are discussed. Through orthogonal decomposition of the output signals, we show that correct information can be retrieved only under specific input. A realistic model with quadruple Helmholtz resonant units is optimally fabricated with the help of a genetic algorithm and is tested both numerically and experimentally. The results are found to be highly consistent with the ideal ones.

II. DESIGN OF IMPEDANCE METASURFACES

A. Modal analysis of the cylindrical shell waveguide

A synthetic presentation of cylindrical shell waveguides is proposed before establishing the impedance metasurfaces. The governing equation for the sound pressure of time-harmonic acoustic waves is

$$(\nabla^2 + \omega^2/c^2)p = 0, \quad (1)$$

where $c = \sqrt{\kappa_0/\rho_0}$ is the velocity of sound in the homogeneous background medium, ω is the operating angular frequency, ρ_0 is the mass density, and κ_0 is the bulk modulus. Cylindrical coordinates are considered in this section. Generally, propagating modes are described explicitly by exact expressions combining Bessel functions. A reduced dimensional approximate solution for cylindrical shell waveguide is proposed instead (see Appendix A for details):

$$p(\rho, \theta, z) = C_m \exp(-\imath(\gamma z + m\theta)) \quad (2)$$

with $\gamma = \sqrt{k_0^2 - m^2/R_0^2}$. Bessel functions are absent from Eq. (2), and each acoustic vortex has a simple analytical expression independent of the radial coordinate. $R_0 = (R_{\text{in}} + R_{\text{out}})/2$ is the arithmetic mean of the inner and outer radii. The wave field depends only on the azimuthal angle θ and on the axial coordinate z .

The axial wavenumber should be real ($\gamma > 0$) for propagating modes, hence

$$|m| < \frac{2\pi R_0}{\lambda_0}. \quad (3)$$

From this expression, the center radius R_0 of the cylindrical shell waveguide required to obtain $N = 2m_{\text{max}} + 1$ propagating wave modes is obtained explicitly. The largest order of propagation m_{max} is smaller than the ratio of the waveguide circumference to the wavelength. Modes such that $|m| > m_{\text{max}}$ are evanescent in the z -direction.

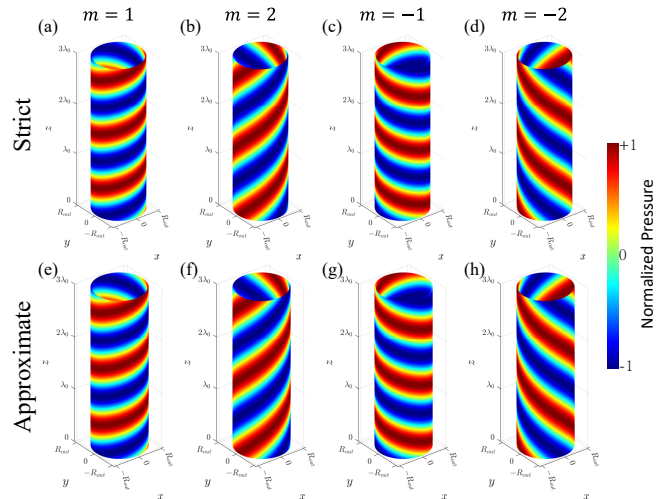


FIG. 1: Spatial distribution of propagating modes at $f_0 = 3500$ Hz in the same cylindrical shell waveguide. The normalized sound pressure of the approximate solutions for (a) $m = 1$, (b) $m = 2$, (c) $m = -1$, and (d) $m = -2$.

For illustration purposes, an example with the following parameters is given in Fig. 1. Air is taken as the background medium, characterized by mass density $\rho_0 = 1.2$ kg/m³ and bulk modulus $\kappa_0 = 0.14$ MPa. Considering the operating frequency $f_0 = \omega/(2\pi) = 3500$ Hz, the wavenumber in air is $k_0 = \omega/c = 64$ m⁻¹ and the wavelength is $\lambda_0 = 9.8$ cm. The inner and outer radii of the waveguide are set to $R_{\text{in}} = 4.45$ cm and $R_{\text{out}} = 4.65$ cm, respectively. Hence, the cylindrical waveguide is very thin. Five mutually orthogonal propagating modes are allowed under this configuration according to Eq. (3). Modes with order $m = \pm 1, \pm 2$ described by the approximate solutions are depicted in Fig. 1, respectively. It can be noticed that guided waves travel along the positive z -axis in the form of acoustic vortices. The chirality of each acoustic vortex is determined by the positive or negative order m , whose absolute value represents the number of periods along the azimuthal direction. A cross-correlation coefficient is computed to measure the quantitative difference between the approximate solution given by Eq.(2) and the exact solution given by Eq.(A9). The cross-correlation coefficient between the two solutions exceeds 99.99% for all four modes. Hence, the reduced dimensional approximation is accurate.

B. Analysis of impedance interface

Our derivation is based on the general principle of impedance theory. Space is assumed to be divided into two domains separated by interface Γ , as shown in Fig. 2. sound pressure fields p_1 and p_2 propagate in the upper and lower regions of space, respectively. Both fields satisfy the scalar Helmholtz Eq. (1). At the interface,

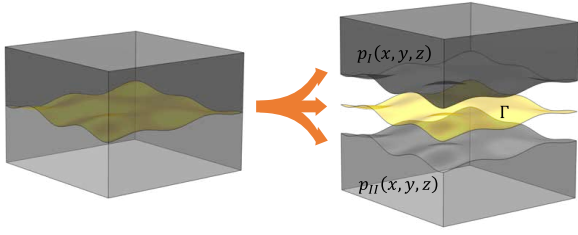


FIG. 2: Illustration of a generalized impedance interface. Space is divided in two domains by interface Γ . Those domains are occupied by pressure fields p_1 and p_2 , respectively.

the impedance relationship is

$$\begin{bmatrix} p_1 \\ p_2 \end{bmatrix} = \begin{bmatrix} Z_{11} & Z_{12} \\ Z_{21} & Z_{22} \end{bmatrix} \begin{bmatrix} -\mathbf{n} \cdot \mathbf{v}_1 \\ \mathbf{n} \cdot \mathbf{v}_2 \end{bmatrix} \text{ on } \Gamma, \quad (4)$$

where \mathbf{v}_i is the local velocity field and \mathbf{n} is the vector normal to the interface and entering region 1. For a conservative system, the real part of the impedance matrix Z vanishes and thus

$$Z = i \begin{bmatrix} X_{11} & X_{12} \\ X_{21} & X_{22} \end{bmatrix}. \quad (5)$$

The target metasurface can then be obtained by approximating the impedance matrix for interface Γ , as given by Eq. (5), with an actual solid structure with a given finite thickness d_s .

The expression of the impedance matrix specific to the case of a single input and a single output acoustic vortices is given by Eq. (B12) in Appendix B1. First, we wish to examine if that expression leads to the successful conversion between two acoustic vortices and for this purpose we evaluate numerically the result of the conversion. The COMSOL Multiphysics software is used in this paper for numerical simulations using the finite element method (FEM). The metasurface is numerically described by a combination of 80 angular units defined using the three-layer model²⁴ (see Appendix B3 for details). The quality of the conversion from the $m_1 = 0$ acoustic vortex to different m_2 acoustic vortices is examined in Fig. 3.

A quantitative evaluation was conducted by evaluating the inner product between the numerical solutions and the theoretical acoustic vortices defined by Eq. (2). Results are displayed as a histogram in Fig. 3(f). All inner products are close to zero except for the diagonal values that are all greater than or equal to 1. As a note, the inner products are not normalized for unit power but to measure the transmission of pressure. Since the mode wavenumber γ_2 decreases with the mode order $|m_2|$ at a given frequency, the propagation speed slows down consequently. Power flow conservation imposes that the power passing through the waveguide cross-section should be equal on both sides of the metasurface in each period, therefore leading to the conservation of

$$\gamma_1 p_1^2 = \gamma_2 p_2^2. \quad (6)$$

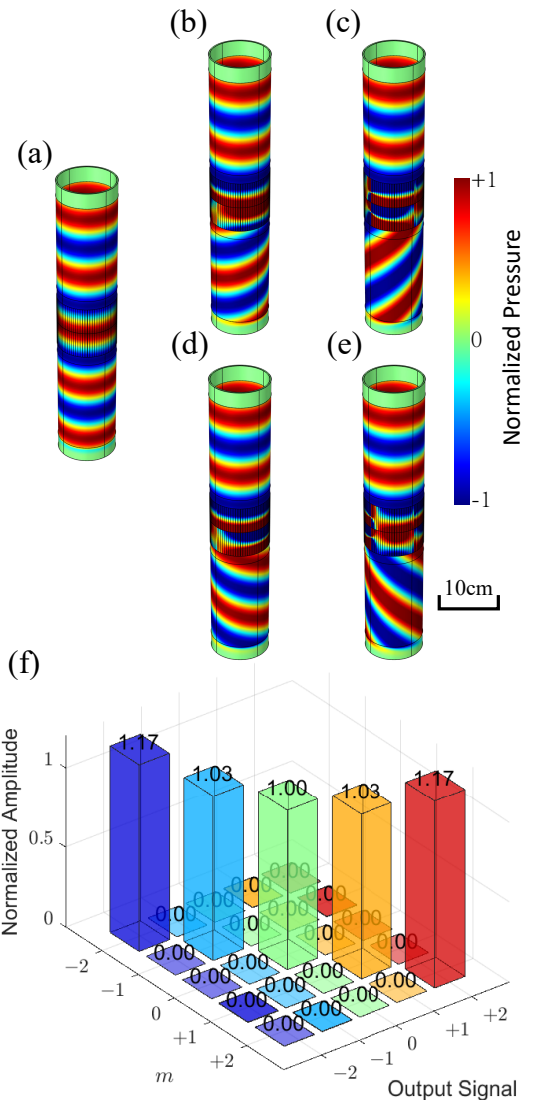


FIG. 3: Conversion of single acoustic vortices at $f_0 = 3500$ Hz, from $m_1 = 0$ to (a) $m_2 = 0$, (b) $m_2 = -1$, (c) $m_2 = -2$, (d) $m_2 = +1$, (e) $m_2 = +2$. (f) Inner products between numerical output wave and the standard acoustic vortices with unit amplitude.

For an input with unitary amplitude ($p_1 = 1$), $p_2 = \sqrt{\gamma_1/\gamma_2} > 1$ when $\gamma_2 < \gamma_1$. The normalized pressure amplitude can then exceed 1²⁴. It is further observed that impedance theory remains valid in the quasi two-dimensional approximation of the problem, despite the application of the reduced dimension approximation.

Next, we consider the more general case of the conversion of a superposition of a set of acoustic vortices to another set. At a given frequency, there are $N = 2m_{\max} + 1$ propagating waves. For $|m| > m_{\max}$, acoustic vortices are evanescent and γ is purely imaginary. Evanescent waves attached to either edge of the metasurface may have to be included in the superpositions in order to satisfy the power flow conservation condition, as exemplified

later. For definiteness, we consider the superposition of α_1 propagating vortices and β_1 evanescent vortices on the incidence side, and the superposition of α_2 propagating vortices and β_2 evanescent vortices on the transmission side. An analysis of the impedance matrix and of power flow conservation is provided in Appendix B 2.

Generally, for an information processing device signals are expected to be input from one side and read from the other side. Therefore, the case of a single input and a double output is demonstrated here ($\alpha_1 = 1, \alpha_2 = 2$). We use again the setting of the previous discussion to provide examples. Three pairs of output acoustic vortices are allowed: $(m_{2,1} = +1, m_{2,2} = -2)$, $(m_{2,1} = +2, m_{2,2} = -2)$ and $(m_{2,1} = +2, m_{2,2} = -1)$ (see Appendix B 2 for details). The consideration of evanescent vortices is essential in order to balance passively the power flow³⁶ ($\beta_1 = 2, \beta_2 = 0$). Numerical simulations for the three metasurfaces implemented with the three-layer model are shown in Fig. 4. The incident flat-phase acoustic vortex is transformed into a pair of acoustic vortices after passing through the metasurface and the evanescent vortices can be observed to decay from the upper edge of the metasurface. The orthogonal decompositions of the output vortices are given in Fig. 4(d). In this case power flow conservation is established as

$$k_0 p_{1,1}^2 = \gamma_{2,1} p_{2,1}^2 + \gamma_{2,2} p_{2,2}^2. \quad (7)$$

It can be verified that conservation is satisfied for the inner products shown in Fig. 4(d). All pressure amplitudes can alternatively be normalized to a sum of 1 for both Fig. 3(f) and Fig. 4(d) by including the power flow in the definition of the inner product, as Appendix D discusses.

C. Series connection of metasurfaces for power flow balance

So far, eight different impedance metasurfaces (five for a single output vortex and three for output vortex pairs) has been considered. It seems difficult to convert an arbitrary input mode to a pair of outputs through a metasurface, since this may result in non-local unit design (see Appendix B 2 for details). The inclusion of evanescent waves also greatly increases the difficulty of design and analytical expressions for impedance matrices is more difficult to obtain. It is however easy to convert any input acoustic vortex into a plane wave, by reciprocity of the result of Sect. II A. Therefore, one can achieve non-local power flow regulation equivalently through series connection of two metasurfaces. The superposition of a plane wave and evanescent waves on one side can fulfill the power flow condition for a pair of acoustic vortices on the other side. concurrently, any single acoustic vortex is obtained owing to the rapid attenuation of evanescent waves. By connecting two metasurfaces in series, in conclusion, any incident acoustic vortex can be converted to a pair of acoustic vortices.

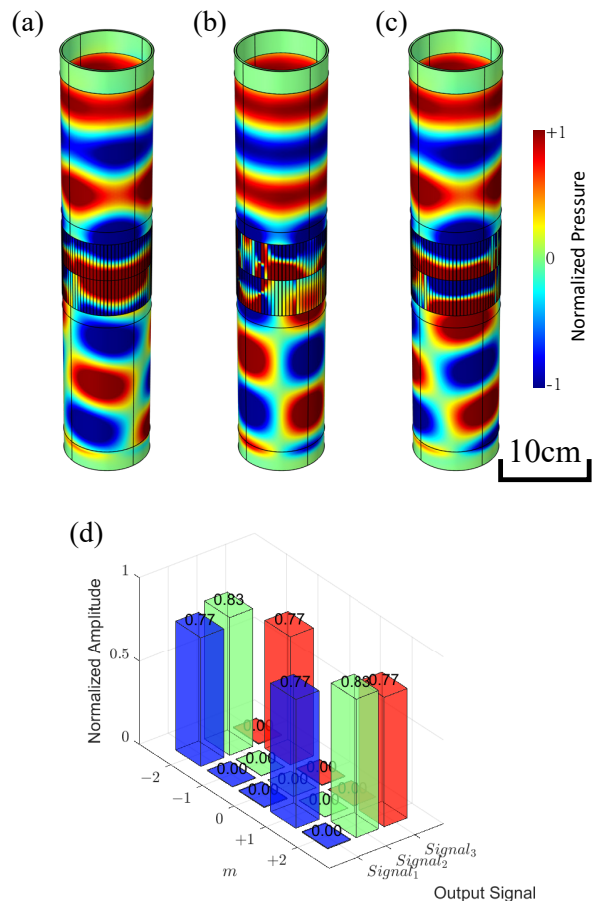


FIG. 4: Conversion from input acoustic vortex $m_1 = 0$ into pairs of acoustic vortices with order: (a) $m_{2,1} = +1, m_{2,2} = -2$, (b) $m_{2,1} = +2, m_{2,2} = -2$, (c) $m_{2,1} = +2, m_{2,2} = -1$. (d) Inner products between numerical output vortices and the standard acoustic vortices with unit amplitude.

The case of input vortex $m_{1,1} = -2$ and output acoustic vortices ($m_{2,1} = -2, m_{2,2} = +2$) is demonstrated as an example in Fig. 5. The input vortex with $m_{1,1} = -2$ is first converted into a plane wave with $m = 0$ and then into the output vortices $m_{2,1} = -2$ and $m_{2,2} = +2$, as shown in Fig. 5(a). The power flow is modulated by the cavity between the two metasurfaces, hence no evanescent waves can be observed at the upper edge of the top metasurface. Power flow conservation is now expressed by the condition

$$\gamma_{1,1} p_{1,1}^2 = \gamma_{2,1} p_{2,1}^2 + \gamma_{2,2} p_{2,2}^2. \quad (8)$$

It can thus be verified that the incident power is exactly distributed to the pair of target modes. If the two metasurfaces are regarded as a whole, non-local transport of power flow is realized in the space between them, even though they are still designed locally.

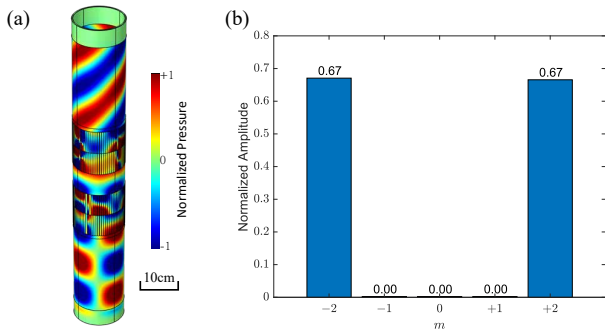


FIG. 5: (a) Conversion from input acoustic vortex with $m_{1,1} = -2$ into a pair of output acoustic vortices with $m_{2,1} = -2$, $m_{2,2} = +2$ using two series-connected metasurfaces. (b) Orthogonal decomposition of the output acoustic vortices with unit amplitude.

III. ANNULAR METASURFACES FOR ENCRYPTED INFORMATION STORAGE

Interface impedance theory may appear at first glance less flexible than the general Snell’s law (see Appendix C for details). Perfect power flow conservation can indeed only be achieved under preset conditions. However, this strict property can in fact be used to produce a cipher lock that only works when the correct input is presented. Following this idea, one may hide information in the metasurface and recover it accurately in the reflected or transmitted acoustic waves. Ideally, the correct information can only be retrieved under a specific incident wave, whereas the output information remains scrambled when the input wave is given incorrectly.

In this section, acoustic vortices are regarded as signals carrying information. An annular metasurface for encrypted information storage is then proposed based on the impedance metasurfaces described in Sect. II C. Information is encoded in the output signal as a superposition of vortices with different amplitudes. A demonstration of a specific case of information reading is examined in the following based on numerical simulations.

The number of allowed propagating waves in the cylindrical shell waveguide is limited by Eq. (3). Besides, due to the requirement on local power flow conservation, there are only eight possible transmission metasurfaces. However, the amplitude ratio $\frac{P_{1,1}}{P_{1,2}}$ is still adjustable, due to the perfect power flow control allowed by impedance theory. In addition, metasurfaces can be stacked angularly as multilayer concentric rings for the sake of integration. Considering those properties, transmitted waves can be related to codes specified by the order and the amplitude of acoustic vortex signals. Sequences composed of four bits are shown in Table I as an example. For convenience, the codes on the right side of the table are termed mode codes, and the codes on the left side are termed binary codes. 8-bit binary codes expressed using two rings can cover the requirements for character encod-

TABLE I: Relationship between binary code and amplitude distribution/mode code.

Binary Code	Amplitude Distribution/ Mode Code				Binary Code	Amplitude Distribution/ Mode Code			
	-2	-1	1	2		-2	-1	1	2
0000	0	0	0	1	1000	1	0	2	0
0001	0	0	1	0	1001	2	0	1	0
0010	0	1	0	0	1010	1	0	3	0
0011	1	0	0	0	1011	3	0	1	0
0100	0	1	0	2	1100	1	0	0	2
0101	0	2	0	1	1101	2	0	0	1
0110	0	1	0	3	1110	1	0	0	3
0111	0	3	0	1	1111	3	0	0	1

ing in ASCII, for instance. The series-connected metasurfaces shown in Fig. 5 could as well be used here for additional encryption. One can write specific information into the metasurface and preset the input acoustic vortex signal according to the above rules.

For demonstration purposes, an example of encrypted storage of three characters is obtained as follows. The word “TJU”, the abbreviation for Tianjin University, is taken as the characters to be encrypted. Their 8-bit binary codes in ASCII are 01010100B, 01001010B and 01010101B, respectively. Each ASCII code is divided into two parts: the high-four bits and the low-four bits, which are encoded into mode codes encoded into two rings. The mode codes corresponding to these characters are listed in Table II. Six layers of concentric cylindrical shell waveguides are adopted, as shown in Fig. 6(a). The waveguides are named Ring₁ to Ring₆ from the outside to the inside, with width $t_w = 0.2$ cm. A rigid wall with thickness $t_c = 0.05$ cm is used as an isolation between each ring. The inner diameter of Ring₆ is set to $D = 6.4$ cm to ensure that $|m_{\max}| = 2$ according to Eq.(3). The input sequence is defined as $M_{\text{input}} = \{m_{1,1}^i | i = 1, \dots, 6\}$, where $m_{1,1}^i$ is the order of the input acoustic vortex signal preset for Ring _{i} . In this example, the input sequence is preset to $M_{\text{input}} = \{-2, -1, +2, +1, +2, -2\}$.

Numerical simulation results for annular metasurfaces designed with the three-layer model are summarized in Fig. 6(b-e). Each ring includes a pair of metasurfaces. The upper metasurface is used to convert the incident acoustic vortex into the fundamental acoustic vortex, whereas the lower metasurface converts the latter into a pair of target acoustic vortices. The encoded characters are hidden in the transmitted waves in the form of mode codes, which can be obtained through orthogonal decomposition. As the example shows, the encrypted characters “TJU” are successfully read out referring to Table I. If the input sequence is wrongly given, for instance as $M'_{\text{input}} = \{+2, +1, -2, -1, -2, +2\}$, the output val-

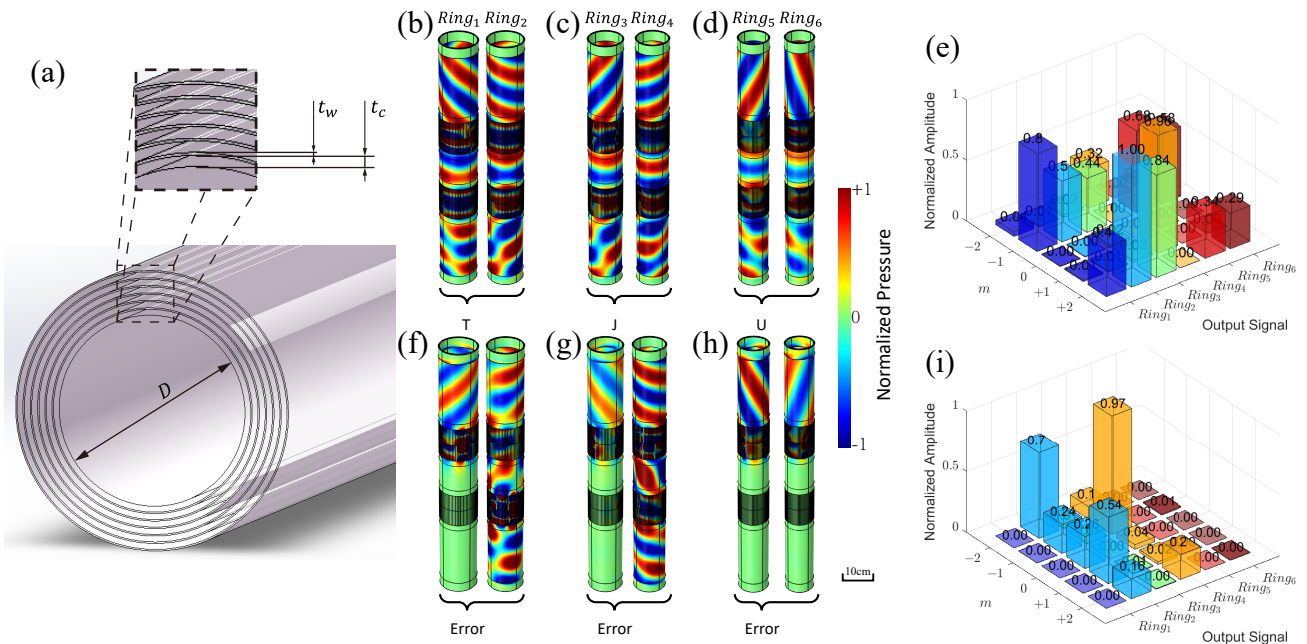


FIG. 6: (a) Schematic diagram of a multilayer coaxial cylindrical shell waveguide. There are 6 concentric annular metasurfaces, with the first and second ring storing the character “T”, the third and fourth ring storing the letter “J”, and the fifth and sixth ring storing the letter “U”. Under the correct input sequence $M_{\text{input}} = \{-2, -1, +2, +1, +2, -2\}$, the response is shown for (b) the first and second ring, (c) the third and fourth ring, (d) the fifth and sixth ring; panel (e) shows the orthogonal decomposition. Under the incorrect input sequence $M'_{\text{input}} = \{+2, +1, -2, -1, -2, +2\}$, the response is shown for (f) the first and second ring, (g) the third and fourth ring, (h) the fifth and sixth ring; panel (i) shows the orthogonal decomposition.

TABLE II: Encoding of characters into mode codes.

Character	Ring Number	Binary Code	Mode Code
T	1	0101	0201
	2	0100	0102
J	3	0100	0102
	4	1010	1030
U	5	0101	0201
	6	0101	0201

ues shown in Figs. 6(f-i) are scrambled. There is hardly any transmitted signal in some of the cylindrical shell waveguides. The upper metasurface actually becomes a filter that blocks the input signal. Some signals can be received at the transmission end in other annular waveguides. However, these signals are not compatible with the encoding principle for ASCII characters in Table I.

IV. OPTIMIZATION OF REAL STRUCTURE AND EXPERIMENTAL VERIFICATION

The three-layer model used in the previous section to implement the impedance matrix is an idealization of an

actual structure. Here, we examine the design of the annular metasurfaces as a physical structure that includes four Helmholtz resonators per unit cell²⁶. A cylindrical shell waveguide with an inner radius $R_{\text{in}} = 3.10$ cm and an outer radius of $R_{\text{out}} = 4.65$ cm is adopted to transmit signals. According to Eq.(3), the highest order of propagation is $|m_{\text{max}}| = 2$. The incident signal is preset as the flat-phase acoustic vortex with $m_{1,1} = 0$. The transmitted signal is considered to implement the binary code “1010”. In the corresponding mode code, the amplitude distribution should be “1030” according to Table I. The components of the target impedance matrix are plotted in Fig. 7(a) as a function of the azimuthal angle. The metasurface is discretized into thirty angular sectors, each of which serves as an independent unit cell. Quadruple Helmholtz resonators are adopted to meet the required impedance characteristics, following the schematic diagram in Fig. 7(b). The detailed parameters of each unit are shown in Figs. 7(c) and (d). The thickness of the metasurface is $d_s = 8.5$ cm. The length and width of the i -th resonant cavity from bottom to top are respectively $l_h = 2$ cm and w_i . Adjacent cavities are separated by a plate with a thickness of 1 mm. The center angle of each sector is $\theta_0 = 360^\circ/30 = 12^\circ$. To ensure independence between adjacent cells, the center angle of each Helmholtz resonator is set to $\theta_h = 9^\circ$. The width of the side channel is w_0 . The neck thickness is $w_t = 2$ mm and the height is h_{t_i} . Among all parameters, w_0 , w_i

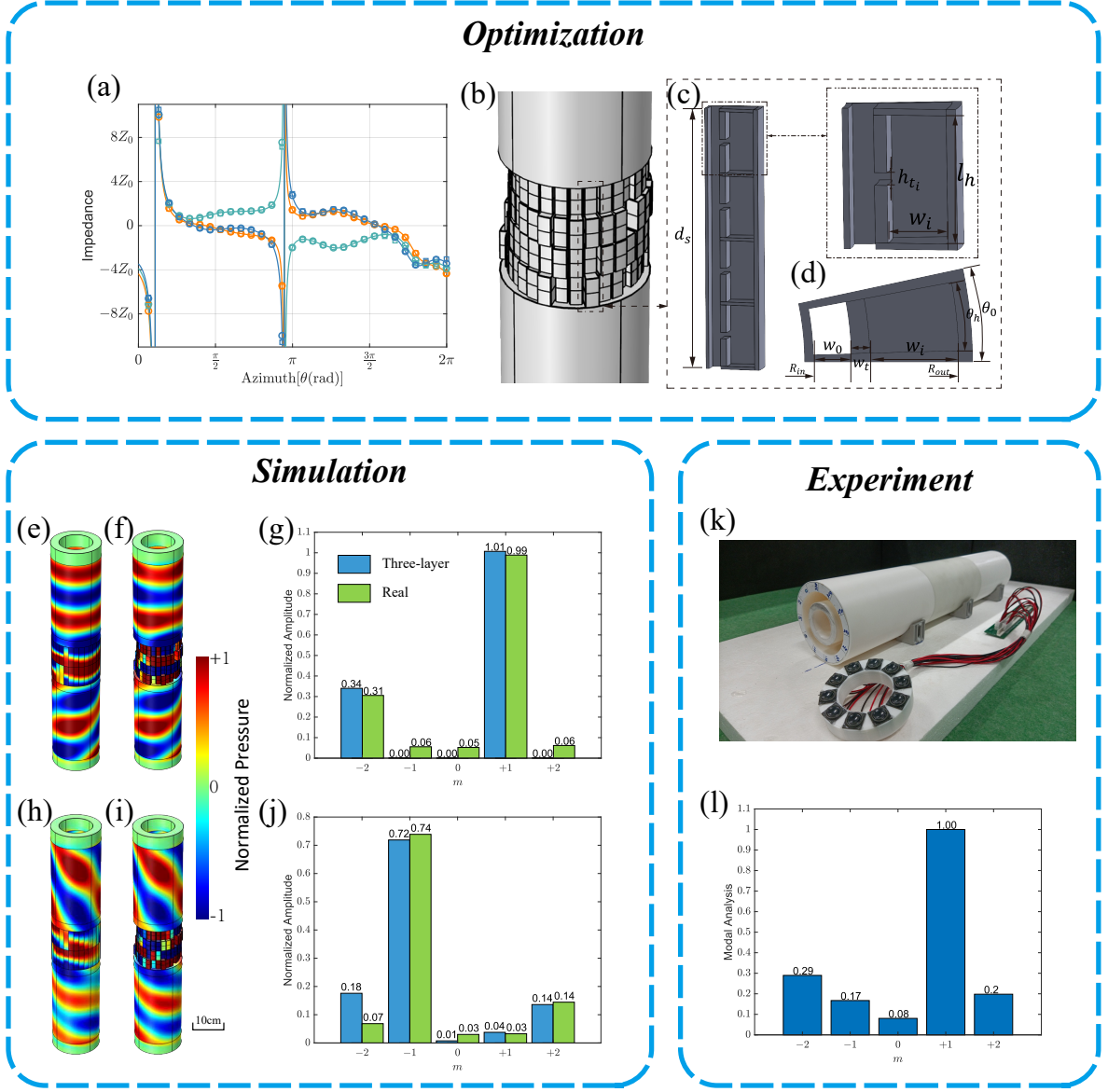


FIG. 7: (a) Analytical results for the required impedance characteristics as a function of azimuthal angle: X_{11} (orange curve), X_{12} (green curve), X_{22} (blue curve). The target impedance characteristics (circular points) and the impedance characteristics of the real structure obtained through optimization (square points) are shown. Schematic diagram of the simulation model of the quadruple Helmholtz resonance metasurface (air); quadruple Helmholtz resonance unit (solid part): (c) side view, (d) vertical view. Response of the metasurfaces under correct input with $m_{1,1} = 0$: (e) by three-layer model, (f) by real structure, (g) orthogonal decomposition. Response of the metasurfaces under incorrect input with $m_{1,1} = 0$: (e) by three-layer model, (f) by real structure, (g) orthogonal decomposition. (k) Photograph of the experimental setup, with speakers and the experimental platform. (l) Modal analysis of experimental data with the least-square method.

and h_{t_i} are then used as optimization variables in a genetic algorithm. The optimization goal is to find a structure best satisfying the target impedance characteristics. All other parameters remain fixed during optimization to avoid considering an excessive solution space. The probabilities of crossover and mutation are set to 20% and 40% respectively. The impedance of the target and of

the real structure obtained after optimization are shown in Fig. 7(a) with circular and square markers, respectively. It can be noted that the impedance characteristics obtained by optimization fairly coincide with the targets and that they are sufficient to represent the curves obtained through analysis. The corresponding structural parameters are listed in Table III.

TABLE III: Parameter configuration of metasurface [Unit: cm].

Cell	w_1	w_2	w_3	w_4	w_t	h_{t_1}	h_{t_2}	h_{t_3}	h_{t_4}
1	0.26	0.29	0.35	0.25	0.9	0.52	1.03	1.41	1.44
2	0.84	0.36	0.81	0.73	0.61	0.20	0.41	1.76	1.79
3	0.75	0.42	0.45	1.12	0.33	0.73	0.84	1.68	1.21
4	0.78	0.76	0.76	0.47	0.44	1.32	1.46	1.58	0.54
5	0.77	0.75	0.89	0.72	0.47	1.56	1.41	1.32	1.62
6	0.40	0.60	0.94	0.39	0.47	0.66	1.17	1.22	0.65
7	0.37	0.77	0.84	0.6	0.49	0.46	1.24	1.49	1.21
8	0.37	0.77	0.84	0.60	0.49	0.40	1.34	1.49	1.26
9	0.30	1.01	0.23	0.54	0.20	1.75	1.41	0.89	1.68
10	0.53	0.86	0.84	0.55	0.50	0.75	1.78	1.33	1.20
11	0.53	0.86	0.84	0.57	0.50	0.75	1.80	1.33	1.26
12	0.92	0.38	0.86	0.40	0.51	1.22	1.18	0.74	1.29
13	0.51	0.76	0.92	0.32	0.53	0.73	1.77	1.32	0.34
14	0.24	0.82	0.61	0.38	0.63	0.87	0.96	1.35	0.32
15	0.86	0.53	0.82	0.44	0.59	1.31	1.54	1.13	1.33
16	0.55	0.38	0.43	0.38	0.65	0.76	0.71	0.73	0.67
17	0.55	0.38	0.43	0.38	0.53	1.23	0.71	1.53	0.67
18	0.49	0.43	0.28	0.30	0.37	1.18	1.66	1.55	0.91
19	0.49	0.43	0.31	0.23	0.37	1.08	1.37	1.48	1.08
20	0.49	0.47	0.40	0.30	0.37	1.22	1.66	1.76	0.96
21	0.61	0.42	0.27	0.30	0.37	1.51	1.76	1.50	0.96
22	0.87	0.53	0.27	0.26	0.58	1.76	1.71	0.71	0.31
23	0.64	0.36	0.28	0.66	0.79	1.51	1.48	0.23	1.34
24	0.61	0.61	0.21	0.55	0.84	1.02	1.42	1.74	1.66
25	0.31	0.33	0.37	0.42	1.03	0.68	0.71	0.84	0.41
26	0.49	0.50	0.20	0.50	0.95	1.09	1.74	0.49	1.80
27	0.23	0.26	0.30	0.40	1.05	1.14	0.42	0.90	0.69
28	0.37	0.31	0.37	0.41	1.04	1.27	1.59	0.58	1.68
29	0.28	0.23	0.42	0.31	1.03	1.74	1.48	1.07	0.35
30	0.38	0.31	0.37	0.30	1.00	1.04	1.63	0.97	1.04

When the correct input signal is given, the response of the theoretical metasurface described by the three-layer model and the response of the quadruple Helmholtz resonator metasurface are in fair agreement (see Figs. 7(e) and (f)). Some reflection occurs at the incident side due to the limitation of structural parameter accuracy. The orthogonally decomposed output signals shown in Figs. 7(g) indicate that the mode code “1030” can be read in either case. Although some of the incident energy leaks into other modes with the quadruple Helmholtz resonator metasurface, the stored information can still be retrieved successfully.

Additionally, we checked the response when the incorrect input $m_{1,1} = -2$ is given (see Fig. 7(h) and (i)). Some reflections can be noticed again. Perfect power flow transmission is no longer satisfied under this input. The orthogonal decomposition of the output signals are shown in Figs. 7(j). The output signals do not match any mode

code in Table I, for both the three-layer model and the quadruple Helmholtz resonator metasurface. The stored binary code “1010” (mode code “1030”) is hence not retrieved.

An experimental verification was conducted for the particular annular metasurface of Fig. 7(b). The experimental setup is depicted in Fig. 7(k). The experimental sample was fabricated by 3D-printing using a photosensitive resin material that can be regarded as a rigid body under the framework of airborne acoustics. Extending on both sides of the sample, two annular waveguides with a wall thickness of 1.5 cm and a length of 20 cm were further fabricated through another 3D-printing technique (polyactic acid; PLA). Geometric and operating parameters were all selected to be consistent with numerical simulations.

Ten input speakers were arranged along a circle and attached tightly at the entrance to ensure that there is no leakage of acoustic power. At the transmission end, a microphone was inserted inside the waveguide at a number of positions to sample the output wavefield. Since there are only five propagating wave modes allowed in the designed waveguide according to Eq.(3), at least five sampling points are required to reconstruct the total field. In order to improve the estimation quality, however, 36 sampling points were defined as follows. Twelve sampling measurement points were evenly distributed along the circumference. Furthermore, considering the possible presence of reflected waves at the exit port, the microphone was inserted axially by 8 cm, 9.5 cm and 11 cm, and the 12 measurements were repeated. The generated and collected signals were controlled by a B&K 3160-A-042 control module connected to a computer. The experiment was repeated ten times before the collected data were subjected to modal analysis with the help of the least-square method. After normalization to the maximum value, the amplitudes assigned to each mode are shown in Fig. 7(l). It can be noted that the amplitude ratio between modes $m = -2$ and $m = +1$ is 0.29, close to the ideal value of 0.33. The amplitude ratios for modes $m = -1$ and $m = 0$ are relatively small, in accordance with the simulation result in Fig. 7(g). However, the amplitude ratio for mode $m = +2$ is about 0.2, about four times more than the numerical simulation result. We attribute this discrepancy to the difficulty to define ideal operating conditions in the experiment. Theoretically, there are only incident waves, whereas in the experiment reflections occur on the speakers. Furthermore, because of the machining accuracy, backscattering in the incidence annular waveguide is bound to occur. As a note, there is almost no way to have the speakers absorb reflected waves, hence some unexpected power leaks into the other modes. It is also worth mentioning that as the thickness of the cylindrical shell decreases, damping near the wall may also take place, especially at high frequencies. In spite of all these limitations, the disturbance could arguably be eliminated at the design and fabrication stage using appropriate methods. Subsequent work

is required to develop more efficient impedance unit models.

V. CONCLUSION

In this paper, we have designed an annular metasurface for encrypted information storage based on impedance metasurface. A cylindrical shell waveguide supporting acoustic vortices is used to carry information. A reduced dimension approximation is introduced to obtain a simpler solution for guided waves and to establish the impedance matrix. Using the strict requirements of impedance theory for input and output fields, the customized binary information stored in the annular metasurfaces can only be read under the incidence of a specific acoustic vortex. Taking the word ‘‘TJU’’ as an example, we demonstrated that characters are read under correct input but are not under incorrect input. Considering the implementation of the metasurface using quadruple Helmholtz resonance units, consistent results are obtained both in simulation and experiment.

Although the discussion was conducted under local design of unit cells, the annular metasurface is not necessarily limited to local power flow transfer. More likely, conversion between acoustic vortices with any different power flow distribution can be realized by metasurfaces with non-local power transfer. Thereby, the capacity of information encryption could be much larger although using a more compact metasurface. Even though only mode codes with specified amplitude ratios were considered, the flexibility of phase difference encoding could still be used to extend the information capacity. This work could also be extended to the design of metasurfaces for acoustic holography. The field of the target images can be series expanded, whereby information could be encrypted and stored in metasurfaces in the form of an image or a two-dimensional array.

Acknowledgments

The authors acknowledge financial support by the National Natural Science Foundation of China (12072223, 12122207, 12021002 and 11991032). V.L. acknowledges financial support by the EIPHI Graduate School (ANR-17-EURE-0002).

Appendix A: Reduced dimensional approximate solution

The Helmholtz equation in cylindrical coordinates is

$$\frac{1}{\rho} \frac{\partial}{\partial \rho} \left(\rho \frac{\partial p}{\partial \rho} \right) + \rho^2 \frac{\partial^2 p}{\partial \theta^2} + \frac{\partial^2 p}{\partial z^2} + k_0^2 p = 0. \quad (\text{A1})$$

Using the method of separation of variables, the analytical solution takes the general form

$$p(\rho, \theta, z) = R(\rho) \Theta(\theta) Z(z). \quad (\text{A2})$$

Substituting this expression into Eq. (A1), wave solutions traveling along the z -axis are solved as

$$\begin{aligned} Z_k &= \exp(-ikz), \\ \Theta_m &= \exp(-im\theta), \\ R_{k,m} &= C_{k,m,1} J_m(\beta\rho) + C_{k,m,2} Y_m(\beta\rho) \end{aligned} \quad (\text{A3})$$

where $k \in \mathbb{R}$, $m \in \mathbb{Z}$, i is the imaginary unit, J_m and Y_m are the m -order Bessel function of the first and second kind, respectively, and

$$\beta^2 = \omega^2/c^2 - k^2. \quad (\text{A4})$$

For cylindrical shell waveguides, Neumann boundary conditions, also termed sound hard boundary conditions, are added at the inner boundary $\rho = R_{\text{in}}$ and at the outer boundary $\rho = R_{\text{out}}$

$$\left. \frac{\partial p}{\partial \rho} \right|_{\rho=R_{\text{in}}} = 0, \quad \left. \frac{\partial p}{\partial \rho} \right|_{\rho=R_{\text{out}}} = 0. \quad (\text{A5})$$

Since Eq. (A5) holds everywhere along the boundaries, each mode (k, m) satisfies

$$C_{k,m,1} J'_m(\beta R_{\text{in}}) + C_{k,m,2} Y'_m(\beta R_{\text{in}}) = 0, \quad (\text{A6})$$

$$C_{k,m,1} J'_m(\beta R_{\text{out}}) + C_{k,m,2} Y'_m(\beta R_{\text{out}}) = 0. \quad (\text{A7})$$

The trivial solution $\beta = 0$ always holds for $m = 0$, associated with a flat phase solution propagating at the velocity of sound ($k = \omega/c$). Furthermore, for a non trivial solution to exist, the transverse wavenumber β must satisfy

$$J'_m(\beta R_{\text{in}}) Y'_m(\beta R_{\text{out}}) - J'_m(\beta R_{\text{out}}) Y'_m(\beta R_{\text{in}}) = 0 \quad (\text{A8})$$

and each mode has the form

$$\begin{aligned} p_{k,m}(\rho, \theta, z) &= [C_{k,m,1} J_m(\beta\rho) + C_{k,m,2} Y_m(\beta\rho)] \\ &\times \exp(-i(kz + m\theta)). \end{aligned} \quad (\text{A9})$$

For different modes $m_1, m_2 \in \mathbb{Z}$, strict orthogonality applies

$$\int_{\Omega} p_{k_1, m_1}(\rho, \theta, z) p_{k_2, m_2}^*(\rho, \theta, z) dV \stackrel{m_1 \neq m_2}{=} 0, \quad (\text{A10})$$

ensuring that the dispersion relation is composed of independent, continuous bands labeled with index m .

Eq. (A8) is an implicit solution for β (or k) for fixed real ω and integer m . The exact solution must be given through Newton iteration method. Propagating solutions require $\beta^2 \geq 0$ or $0 \leq k^2 \leq \omega^2/c^2$. Hence the condition

$$|k_{\omega, m}| \leq \omega/c \quad (\text{A11})$$

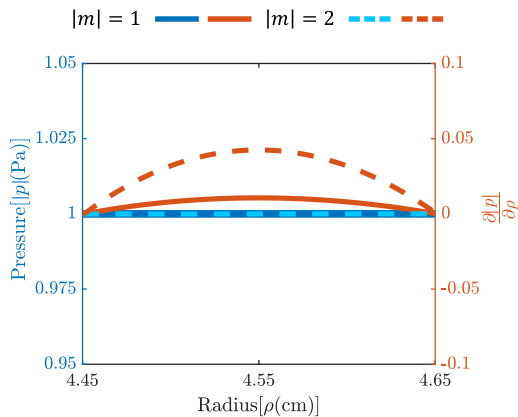


FIG. 8: The radial cross-sections of normalized pressure $\frac{|p|}{p_0}$ (blue curve for $|m| = 1$, blue dashed curve for $|m| = 2$) and pressure gradient $\frac{R_0}{p_0} \frac{\partial |p|}{\partial \rho}$ (red curve for $|m| = 1$, red dashed curve for $|m| = 2$) of the exact solution [Eq.(A9)].

TABLE IV: Characteristics of propagating modes at $f_0 = 3500$ Hz in the cylindrical shell waveguide with $R_{\text{in}} = 4.45$ cm and $R_{\text{out}} = 4.65$ cm.

m	β (m ⁻¹)	k (m ⁻¹)	$C_{k,m,2}/C_{k,m,1}$
0	0	64	0
± 1	21.9798	60.1073	-0.3736
± 2	43.9596	46.5140	-0.4375

limits the number of propagating modes at a specific frequency and is used to filter the results. The allowed modes and corresponding parameters are listed in Table IV. Five mutually orthogonal propagating modes are allowed for the waveguide under this configuration.

It can be noted that the solution of Eqs. (A7-A9) is implicit and does not allow for analytic solutions. Furthermore, the number of propagating modes for a given structure size at every frequency is only obtained numerically, which introduces difficulties for the subsequent analysis of the impedance interface. However, it can be noticed in Fig. 8 that the normalized complex pressure $\frac{p}{p_0}$ is almost constant along the radial direction. The same observation holds for the normalized complex pressure gradient $\frac{R_0}{p_0} \frac{\partial p}{\partial \rho}$, where $R_0 = (R_{\text{in}} + R_{\text{out}})/2$ is the arithmetic mean of the inner and outer radii. Therefore, an approximate solution can be proposed to obtain simpler expressions. It is observed that the azimuthal phase gradient that characterizes acoustic vortices is properly maintained during this approximation process^{37,38}.

Considering $\Delta R = R_{\text{out}} - R_{\text{in}} \ll \lambda_0$ together with the boundary conditions Eqs. (A5-A6), the following approximation is considered

$$\frac{\partial p}{\partial \rho} \approx 0, \quad \frac{\partial^2 p}{\partial \rho^2} \approx 0. \quad (\text{A12})$$

Then Eq. (A1) becomes

$$\frac{1}{R_0^2} \frac{\partial^2 p}{\partial \theta^2} + \frac{\partial^2 p}{\partial z^2} + k_0^2 p = 0 \quad (\text{A13})$$

and the pressure distribution does not depend on ρ anymore. Using again the method of separation of variables, the general solution is assumed to take the form

$$p(\rho, \theta, z) = \Theta(\theta) Z(z) \quad (\text{A14})$$

and Eq. (A13) decouples into

$$\frac{d^2 \Theta}{d\theta^2} + m^2 \Theta = 0, \quad (\text{A15})$$

$$\frac{d^2 Z_m}{dz^2} + (\omega^2/c^2 - m^2/R_0^2) Z_m = 0. \quad (\text{A16})$$

Modes propagating along the positive z -direction satisfy the relation

$$\omega > |m|c/R_0. \quad (\text{A17})$$

We introduce the notation $\gamma_i = \sqrt{k_0^2 - m_i^2/R_0^2}$ as the longitudinal wavenumber. The approximate solution can then be given as

$$p(\theta, z) = C_m \exp(-i(\gamma z + m\theta)). \quad (\text{A18})$$

The radius coordinate ρ disappears in the approximate expression, whereas the azimuthal phase gradient that characterizes acoustic vortices is maintained. This approximation is of great help for establishing impedance metasurfaces in the main text.

Appendix B: Impedance matrices of metasurfaces

1. Impedance metasurfaces with single input and single output

In the frequency domain, the local velocity of the acoustic field is obtained from the pressure field p_i as

$$\mathbf{v}_i = \frac{i}{\omega_0 \rho_0} \nabla p_i, \quad i = 1, 2. \quad (\text{B1})$$

Then the power flow vector is

$$\mathbf{I}_i = \frac{1}{2} \text{Re} [p_i \mathbf{v}_i^*], \quad i = 1, 2. \quad (\text{B2})$$

This physical quantity is crucial in the following analysis. Power flow conservation needs to be satisfied on the interface

$$\int_{\Gamma} \frac{1}{2} \text{Re} [p_1 (\mathbf{n} \cdot \mathbf{v}_1^*)] dS = \int_{\Gamma} \frac{1}{2} \text{Re} [p_2 (\mathbf{n} \cdot \mathbf{v}_2^*)] dS. \quad (\text{B3})$$

In order to ensure an independent design of all metasurface units in the following text, the transfer of power

flow is expected to be local. Then, Eq. (B3) should be restricted to

$$\frac{1}{2}\text{Re}[p_1(\mathbf{n} \cdot \mathbf{v}_1^*)] = \frac{1}{2}\text{Re}[p_2(\mathbf{n} \cdot \mathbf{v}_2^*)]. \quad (\text{B4})$$

Combining Eqs. (B1-B4), it follows

$$X_{12} = X_{21}. \quad (\text{B5})$$

This relation indicates that after considering the localized power flow Eq. (B4), the impedance matrix is symmetric.

Let us focus on the conversion between two different acoustic vortices in a cylindrical shell waveguide. A plane described by

$$z = 0, \quad (\text{B6})$$

with normal vector

$$\mathbf{n} = \mathbf{e}_z. \quad (\text{B7})$$

is adopted for Γ . The azimuthal orders of the input and the output vortices are denoted m_1 and m_2 , respectively. The acoustic fields on both sides of the metasurface then read

$$p_1 = p_0 \exp(-\iota(\gamma_1 z + m_1 \theta)), \quad (\text{B8})$$

$$p_2 = Ap_0 \exp(-\iota(\gamma_2 z + m_2 \theta)), \quad (\text{B9})$$

and their velocity vectors read

$$\mathbf{v}_1 = \frac{p_0}{Z_0 k_0} \exp(-\iota(\gamma_1 z + m_1 \theta)) (\gamma_1 \mathbf{e}_z + m_1/R_0 \mathbf{e}_\theta), \quad (\text{B10})$$

$$\mathbf{v}_2 = \frac{Ap_0}{Z_0 k_0} \exp(-\iota(\gamma_2 z + m_2 \theta)) (\gamma_2 \mathbf{e}_z + m_2/R_0 \mathbf{e}_\theta), \quad (\text{B11})$$

where $Z_0 = c_0 \rho_0$ is the acoustic impedance of air. Eq. (B4) is used to ensure localized power flow. Substituting expressions into Eq. (4) and following the same steps as in Ref. 26, the impedance matrix can be easily solved as

$$Z = \iota \begin{bmatrix} \frac{Z_0 k_0}{\gamma_1} \cot(\Delta m \theta) & \frac{Z_0 k_0}{\sqrt{\gamma_1 \gamma_2}} \csc(\Delta m \theta) \\ \frac{Z_0 k_0}{\sqrt{\gamma_1 \gamma_2}} \csc(\Delta m \theta) & \frac{Z_0 k_0}{\gamma_2} \cot(\Delta m \theta) \end{bmatrix}, \quad (\text{B12})$$

with $\Delta m = m_1 - m_2$ and the amplitude amplification factor

$$A = \sqrt{\frac{\gamma_1}{\gamma_2}}. \quad (\text{B13})$$

2. Impedance metasurfaces with single input and double output

The acoustic pressure distributions are expressed as

$$p_1 = \sum_{i=1}^{\alpha_1} p_{1,i} \exp(-\iota(\gamma_{1,i} z + m_{1,i} \theta + \varphi_{1,i})) + \sum_{i=1}^{\beta_1} p_{1,i}^e \exp(-k_{1,i}^e z - m_{1,i}^e \theta - \iota \varphi_{1,i}^e), \quad (\text{B14})$$

$$p_2 = \sum_{i=1}^{\alpha_2} p_{2,i} \exp(-\iota(\gamma_{2,i} z + m_{2,i} \theta + \varphi_{2,i})) + \sum_{i=1}^{\beta_2} p_{2,i}^e \exp(k_{2,i}^e z - m_{2,i}^e \theta - \iota \varphi_{2,i}^e). \quad (\text{B15})$$

The velocity vectors read

$$v_1 = \left[\sum_{i=1}^{\alpha_1} \frac{p_{1,i} m_{1,i}}{Z_0 k_0 R_0} \exp(-\imath(\gamma_{1,i} z + m_{1,i} \theta + \varphi_{1,i})) + \sum_{i=1}^{\beta_1} \frac{p_{1,i}^e m_{1,i}^e}{Z_0 k_0 R_0} \exp(-k_{1,i}^e z - \imath m_{1,i}^e \theta - \imath \varphi_{1,i}^e) \right] \mathbf{e}_\theta + \left[\sum_{i=1}^{\alpha_1} \frac{p_{1,i} \gamma_{1,i}}{Z_0 k_0} \exp(-\imath(\gamma_{1,i} z + m_{1,i} \theta + \varphi_{1,i})) + \sum_{i=1}^{\beta_1} \frac{-\imath p_{1,i}^e k_{1,i}^e}{Z_0 k_0} \exp(-k_{1,i}^e z - \imath m_{1,i}^e \theta - \imath \varphi_{1,i}^e) \right] \mathbf{e}_z, \quad (\text{B16})$$

$$v_2 = \left[\sum_{i=1}^{\alpha_2} \frac{p_{2,i} m_{2,i}}{Z_0 k_0 R_0} \exp(-\imath(\gamma_{2,i} z + m_{2,i} \theta + \varphi_{2,i})) + \sum_{i=1}^{\beta_2} \frac{p_{2,i}^e m_{2,i}^e}{Z_0 k_0 R_0} \exp(k_{2,i}^e z - \imath m_{2,i}^e \theta - \imath \varphi_{2,i}^e) \right] \mathbf{e}_\theta + \left[\sum_{i=1}^{\alpha_2} \frac{p_{2,i} \gamma_{2,i}}{Z_0 k_0} \exp(-\imath(\gamma_{2,i} z + m_{2,i} \theta + \varphi_{2,i})) + \sum_{i=1}^{\beta_2} \frac{\imath p_{2,i}^e k_{2,i}^e}{Z_0 k_0} \exp(k_{2,i}^e z - \imath m_{2,i}^e \theta - \imath \varphi_{2,i}^e) \right] \mathbf{e}_z. \quad (\text{B17})$$

For evanescent waves, the following condition holds

$$|m_{1,i}^e| > 2\pi R_0/\lambda_0, |m_{2,i}^e| > 2\pi R_0/\lambda_0. \quad (\text{B18})$$

Next, conservation of power flow [Eq. (B4)] is imposed along the normal direction \vec{n} to the metasurface Γ , leading to

$$\begin{aligned} & \sum_i^{\alpha_1} \sum_l^{\alpha_1} \gamma_{1,l} p_{1,i} p_{1,l} \cos[(m_{1,l} - m_{1,i})\theta - (\varphi_{1,l} - \varphi_{1,i})] - \sum_i^{\alpha_1} \sum_l^{\beta_1} k_{1,l}^e p_{1,i} p_{1,l}^e \sin[(m_{1,l}^e - m_{1,i})\theta - (\varphi_{1,l}^e - \varphi_{1,i})] \\ & + \sum_i^{\beta_1} \sum_l^{\alpha_1} \gamma_{1,l} p_{1,i}^e p_{1,l} \cos[(m_{1,l} - m_{1,i}^e)\theta - (\varphi_{1,l} - \varphi_{1,i}^e)] - \sum_i^{\beta_1} \sum_l^{\beta_1} k_{1,l}^e p_{1,i}^e p_{1,l}^e \sin[(m_{1,l}^e - m_{1,i}^e)\theta - (\varphi_{1,l}^e - \varphi_{1,i}^e)] \\ & = \sum_i^{\alpha_2} \sum_l^{\alpha_2} \gamma_{2,l} p_{2,i} p_{2,l} \cos[(m_{2,l} - m_{2,i})\theta - (\varphi_{2,l} - \varphi_{2,i})] + \sum_i^{\alpha_2} \sum_l^{\beta_2} k_{2,l}^e p_{2,i} p_{2,l}^e \sin[(m_{2,l}^e - m_{2,i})\theta - (\varphi_{2,l}^e - \varphi_{2,i})] \\ & + \sum_i^{\beta_2} \sum_l^{\alpha_2} \gamma_{2,l} p_{2,i}^e p_{2,l} \cos[(m_{2,l} - m_{2,i}^e)\theta - (\varphi_{2,l} - \varphi_{2,i}^e)] + \sum_i^{\beta_2} \sum_l^{\beta_2} k_{2,l}^e p_{2,i}^e p_{2,l}^e \sin[(m_{2,l}^e - m_{2,i}^e)\theta - (\varphi_{2,l}^e - \varphi_{2,i}^e)]. \end{aligned} \quad (\text{B19})$$

Generally speaking, solutions to this equation can be obtained by equating the coefficients of each trigonometric function, since they are orthogonal. However, there are an infinite number of solutions since the number of variables is far larger than the number of equations. For definiteness, we would like to consider in the following solutions describing the conversion of a single fundamental vortex ($\alpha_1 = 1$, $m_{1,1} = 0$) to a pair of propagating vortices ($\alpha_2 = 2$, $\beta_2 = 0$). The reference of phase is the incident vortex, or $\varphi_{1,1} = 0$. For reasons that will soon be apparent, we have to include a pair of evanes-

cent vortices ($\beta_1 = 2$) with opposite azimuthal numbers ($m_{1,1}^e = -m_{1,2}^e$). From (B4) we must have

$$\begin{aligned} p_{1,1}^e &= p_{1,2}^e \\ k_{1,1}^e &= k_{1,2}^e \\ m_{1,1}^e &= -m_{1,2}^e \\ \varphi_{1,1}^e &= -\varphi_{1,2}^e \end{aligned} \quad (\text{B20})$$

The power flow conservation (B19) becomes

$$\begin{aligned} & p_{1,1}^2 + 2p_{1,1}^e p_{1,1} \cos(m_{1,1}^e \theta - \varphi_{1,1}^e) \\ & = \frac{\gamma_{2,1}}{k_0} p_{2,1}^2 + \frac{\gamma_{2,2}}{k_0} p_{2,2}^2 + \frac{(\gamma_{2,2} + \gamma_{2,1})}{k_0} p_{2,1} p_{2,2} \cos[(m_{2,2} - m_{2,1})\theta - (\varphi_{2,2} - \varphi_{2,1})]. \end{aligned} \quad (\text{B21})$$

The coefficients of each term on both sides must be equal, from the orthogonality of trigonometric functions. Con-

servation of power flow is guaranteed for any θ when

$$1 = \frac{\gamma_{2,1}}{k_0} \left(\frac{p_{2,1}}{p_{1,1}} \right)^2 + \frac{\gamma_{2,2}}{k_0} \left(\frac{p_{2,2}}{p_{1,1}} \right)^2, \quad (\text{B22})$$

$$p_{1,1}^e = \frac{\gamma_{2,1} + \gamma_{2,2}}{k_0} \frac{p_{2,1} p_{2,2}}{2p_{1,1}}, \quad (\text{B23})$$

$$m_{1,1}^e = m_{2,2} - m_{2,1}, \quad (\text{B24})$$

$$\varphi_{1,1}^e = \varphi_{2,2} - \varphi_{2,1}. \quad (\text{B25})$$

The last equation is valid modulo 2π . Through Eq. (4), the required metasurface is given by interface impedance

$$X_{11} = [p_{2,1} \cos(\Phi_{2,1}) \gamma_{2,1} + p_{2,2} \cos(\Phi_{2,2}) \gamma_{2,2}] [2p_{1,1}^e \cos(\Phi_{1,1}^e) + p_{1,1}] k_0 Z_0 / D, \quad (\text{B26})$$

$$X_{12} = [2p_{1,1}^e \cos(\Phi_{1,1}^e) + p_{1,1}] k_0^2 p_{1,1} Z_0 / D, \quad (\text{B27})$$

$$X_{21} = [\gamma_{2,1} p_{2,1}^2 + \gamma_{2,2} p_{2,2}^2 + (\gamma_{2,2} + \gamma_{2,1}) p_{2,1} p_{2,2} \cos(\Phi_{2,2} - \Phi_{2,1})] k_0 Z_0 / D, \quad (\text{B28})$$

$$X_{22} = \{ [p_{2,1} \cos(\Phi_{2,1}) + p_{2,2} \cos(\Phi_{2,2})] p_{1,1} k_0 + 2p_{1,1}^e k_{1,1}^e \cos(\Phi_{1,1}^e) [p_{2,1} \sin(\Phi_{2,1}) + p_{2,2} \sin(\Phi_{2,2})] \} k_0 Z_0 / D, \quad (\text{B29})$$

$$D = [p_{2,1} \sin(\Phi_{2,1}) \gamma_{2,1} + p_{2,2} \sin(\Phi_{2,2}) \gamma_{2,2}] p_{1,1} k_0 - 2p_{1,1}^e k_{1,1}^e \cos(\Phi_{1,1}^e) [p_{2,1} \cos(\Phi_{2,1}) \gamma_{2,1} + p_{2,2} \cos(\Phi_{2,2}) \gamma_{2,2}] \quad (\text{B30})$$

where

$$\Phi_{2,1} = \varphi_{2,1} - m_{2,1} \theta, \quad (\text{B31})$$

$$\Phi_{2,2} = \varphi_{2,2} - m_{2,2} \theta, \quad (\text{B32})$$

$$\Phi_{1,1}^e = \varphi_{1,1}^e - m_{1,1}^e \theta. \quad (\text{B33})$$

As a note, the symmetry [Eq. (B5)] still holds when combining Eqs. (B27) and (B28) together with Eq. (B22). Due to the constraint set by Eq. (B18), the acoustic vortices satisfy

$$m_{1,1}^e = m_{2,2} - m_{2,1} > 2\pi R_0. \quad (\text{B34})$$

Their phases are set as

$$\varphi_{2,1} = \varphi_{2,2} = \varphi_{1,1}^e = 0 \quad (\text{B35})$$

for simplicity. Imposing $p_{2,1} = p_{2,2}$, Eq. (B22) yields

$$p_{2,1} = p_{2,2} = \frac{p_{1,1}}{\sqrt{(\gamma_{2,1} + \gamma_{2,2})/k_0}}. \quad (\text{B36})$$

3. Three-layer model for simulation

The three-layer model used in numerical simulations is set according to the following principles. Adjacent units are separated by sound-hard boundaries. Each unit contains three interior impedance boundaries separated by distance $d_0 = 4.25$ cm, set according to

$$Z_1 = Z_{11} + Z_{12} + \imath Z_0 \cot(k_0 d_0), \quad (\text{B37})$$

$$Z_2 = 2\imath Z_0 \cot(k_0 d_0) - \frac{Z_0^2}{Z_{12}} \sin^{-2}(k_0 d_0), \quad (\text{B38})$$

$$Z_3 = Z_{22} + Z_{12} + \imath Z_0 \cot(k_0 d_0), \quad (\text{B39})$$

respectively²⁴. The thickness of the metasurface satisfies $d_s = 2d_0 = 8.5$ cm. Perfectly matched layers are added to both ends of the waveguide to avoid reflections. The maximum element size in the finite element mesh is set to $\lambda_0/10$ to ensure convergence. Additional mesh refinement is applied near the impedance boundaries. The background pressure field representing the incident wave travels along the negative z -axis, with unitary amplitude.

Appendix C: A drawback of impedance theory

1. Semi-infinite space

In impedance theory, both the background field and the metasurface are considered as a single complete system. In the two-dimensional case the background field is an infinite plane wave

$$p(x, y) = C_0 \exp(-\imath(k_x x + k_y y)). \quad (\text{C1})$$

The analysis of the 2D impedance interface was carried out by Díaz-Rubio et al.²⁴ and Peng et al.²⁹.

However, a Gaussian envelope must be used in order to truncate laterally wavefields in practice³⁶, in the form

$$p(x, y) = C_0 G(f(x, y), \sigma) \exp(-\imath(k_x x + k_y y)), \quad (\text{C2})$$

where $G(u, \sigma)$ is a Gaussian function with σ the variance used to describe the lateral extent of the wave and where

$$f(x, y) = -k_x y + k_y x + b_0 \quad (\text{C3})$$

is the center line of the incident wave. Hence, when the incident field is adjusted to Eq. (C2), the distribution of the power flow

$$\mathbf{I} = \frac{1}{2} \text{Re}[p \mathbf{v}^*] \quad (\text{C4})$$

should be adjusted as well. As a result, it might be more difficult to balance the power flow at incident and transmission boundaries, especially for application to beam splitting³⁶. Although the result looks visually correct, the observation of plane wave propagation is not perfect in a strict sense.

It needs to be noted that Eq. (2) and Eq. (C1) are similar in form. The former, however, describes a wave field that is bounded in space by natural boundary conditions and that does not require lateral truncation as the latter does. Theoretically, the potential of impedance theory can hence be fully exploited in cylindrical shell waveguides where perfect power flow regulation can be achieved.

2. Strict input requirements

Acoustic impedance theory appears to be less flexible than generalized Snell's law despite its perfect manipulation of the power flow. One could alternatively fabricate a metasurface based on generalized Snell's law⁵ providing a local phase-shift in transmission

$$\Phi(x) = \alpha k_0 x. \quad (\text{C5})$$

For input incident waves with incident angles θ_{i1} and θ_{i2} , the transmission angle of the response can be determined as

$$\theta_{t1} = \arcsin(\alpha - \sin \theta_{i1}), \quad (\text{C6})$$

$$\theta_{t2} = \arcsin(\alpha - \sin \theta_{i2}), \quad (\text{C7})$$

respectively. But when it comes to impedance theory, these two sets of angles would correspond to completely different metasurfaces²⁴. Therefore, it is evident that impedance theory is hardly applicable for a wide-angle response. In the case of annular waveguides, the response is deeply modified when the input is wrongly given. Perfect power flow conservation can only be achieved under preset conditions.

Appendix D: Normalization of modes

The inner product of the acoustic vortex described by Eq. (2) is defined in this paper as

$$I_i = \langle p_2, p_s^i \rangle = \frac{1}{V} \int_V p_2 \cdot \exp(\iota(\gamma_i z + m_i \theta)) dv. \quad (\text{D1})$$

where p_s^i is the standard vortex with order m_i . Clearly this definition considers only pressure and not velocity, so that the sum of output amplitudes may exceed 1 even though transmittance of power flow is 100% or less. One could instead adopt a definition of the inner product induced by power flow conservation. For the case of single

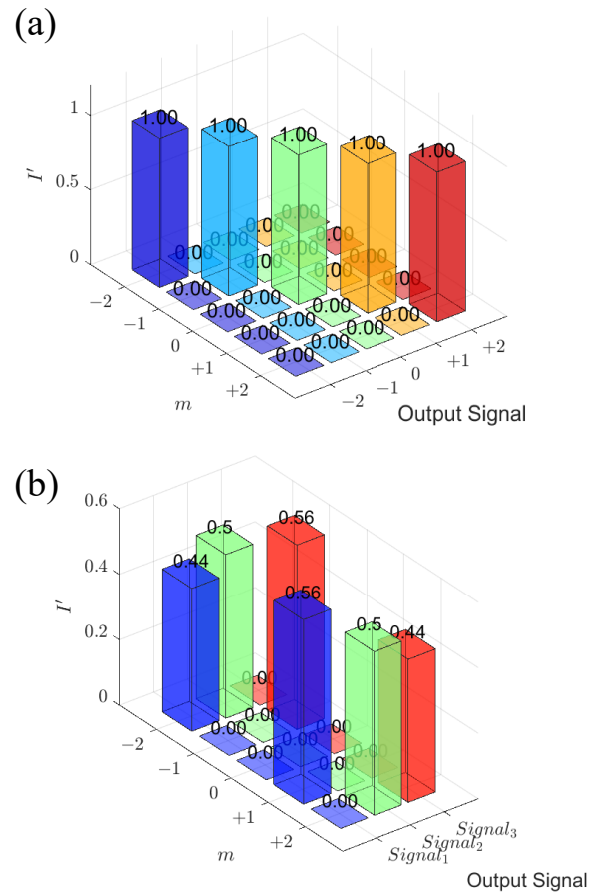


FIG. 9: Mode analysis given by power induced inner product (a) single output, (b) double output.

input to multiple outputs, the conservation of power flow on both sides of the metasurface reads

$$\gamma_1 p_1^2 = \sum_{i=1}^{\alpha_2} \gamma_{2,i} p_{2,i}^2. \quad (\text{D2})$$

Normalizing with reference to the input power $\gamma_1 p_1^2$, the inner product would then be defined as

$$I'_i = \langle p_2, p_s^i \rangle = \frac{\gamma_i}{V} \int_V p_2 \cdot \exp(-\iota(\gamma_i z + m_i \theta)) dv. \quad (\text{D3})$$

Under this definition, the sum of amplitudes becomes

$$\sum_{i=1}^{\alpha_2} I'_i = \sum_{i=1}^{\alpha_2} \langle p_2, p_s^i \rangle = 1. \quad (\text{D4})$$

Modal analysis obtained given by Eq. (D4) for the examples of Figs. 3 and 4 is presented in Fig. 9. The sums of amplitudes all become 1. Another issue however arises when there are multiple output vortices. The normalized amplitudes of modes $m_{2,1} = -1$ and $m_{2,2} = 2$ are not equal in Fig. 9(b) when $p_{2,1}$ and $p_{2,2}$ are selected to be equal. Therefore, the usual inner product definition of

Eq. (D1), originating from plane waves, was still adopted in this paper to define amplitude ratios, without loss of

generality.

-
- * Electronic address: wangyanfeng@tju.edu.cn
- ¹ Y.-F. Wang, Y.-Z. Wang, B. Wu, W. Chen, and Y.-S. Wang, *Applied Mechanics Reviews* **72**, 040801 (2020).
 - ² N. Yu, P. Genevet, M. A. Kats, F. Aieta, J.-P. Tetienne, F. Capasso, and Z. Gaburro, *science* **334**, 333 (2011).
 - ³ Y. Li, B. Liang, Z.-m. Gu, X.-y. Zou, and J.-c. Cheng, *Scientific reports* **3**, 2546 (2013).
 - ⁴ J. Mei and Y. Wu, *New Journal of Physics* **16**, 123007 (2014).
 - ⁵ Z. Shen and D. Huang, *Nanomanufacturing* **2**, 194 (2022).
 - ⁶ S. Yang, J. Wang, G. Dai, F. Yang, and J. Huang, *Physics Reports* **908**, 1 (2021).
 - ⁷ G. W. Milton, M. Briane, and J. R. Willis, *New Journal of Physics* **8**, 248 (2006).
 - ⁸ Y.-Z. Tian, Y.-F. Wang, G.-Y. Huang, V. Laude, and Y.-S. Wang, *International Journal of Heat and Mass Transfer* **195**, 123128 (2022).
 - ⁹ Y. Zhu and B. Assouar, *Physical Review Materials* **3**, 045201 (2019).
 - ¹⁰ M. Golub, *Journal of Applied Mechanics and Technical Physics* **57**, 1190 (2016).
 - ¹¹ M. Xiao, X. Wang, H. Ma, and W. Zhang, *High Voltage* **7**, 586 (2022).
 - ¹² T. J. Cui, M. Q. Qi, X. Wan, J. Zhao, and Q. Cheng, *Light: science & applications* **3**, e218 (2014).
 - ¹³ H. Yasuda, P. R. Buskohl, A. Gillman, T. D. Murphey, S. Stepney, R. A. Vaia, and J. R. Raney, *Nature* **598**, 39 (2021).
 - ¹⁴ C. Li, Z.-K. Peng, and Q. He, *Matter* **5**, 988 (2022).
 - ¹⁵ B. Assouar, B. Liang, Y. Wu, Y. Li, J.-C. Cheng, and Y. Jing, *Nature Reviews Materials* **3**, 460 (2018).
 - ¹⁶ H.-T. Zhou, S.-C. Zhang, T. Zhu, Y.-Z. Tian, Y.-F. Wang, and Y.-S. Wang, *Advanced Science* p. 2207181 (2023).
 - ¹⁷ Z. Cai, S. Zhao, Z. Huang, Z. Li, M. Su, Z. Zhang, Z. Zhao, X. Hu, Y.-S. Wang, and Y. Song, *Advanced Functional Materials* **29**, 1906984 (2019).
 - ¹⁸ F. Liu, W. Li, Z. Pu, and M. Ke, *Applied Physics Letters* **114**, 193501 (2019).
 - ¹⁹ I. Rondón and D. Leykam, *Journal of Physics: Condensed Matter* **32**, 104001 (2019).
 - ²⁰ K. Wu, J.-J. Liu, Y.-j. Ding, W. Wang, B. Liang, and J.-C. Cheng, *Nature communications* **13**, 5171 (2022).
 - ²¹ X. Jiang, Y. Li, B. Liang, J.-c. Cheng, and L. Zhang, *Physical review letters* **117**, 034301 (2016).
 - ²² X. Jiang, B. Liang, J.-C. Cheng, and C.-W. Qiu, *Advanced Materials* **30**, 1800257 (2018).
 - ²³ Z. Sun, Y. Shi, X. Sun, H. Jia, Z. Jin, K. Deng, and J. Yang, *Journal of Physics D: Applied Physics* **54**, 205303 (2021).
 - ²⁴ A. Díaz-Rubio and S. A. Tretyakov, *Physical Review B* **96**, 125409 (2017).
 - ²⁵ V. S. Asadchy, M. Albooyeh, S. N. Tsvetkova, A. Díaz-Rubio, Y. Ra'di, and S. Tretyakov, *Physical Review B* **94**, 075142 (2016).
 - ²⁶ J. Li, C. Shen, A. Díaz-Rubio, S. A. Tretyakov, and S. A. Cummer, *Nature communications* **9**, 1342 (2018).
 - ²⁷ A. Díaz-Rubio, J. Li, C. Shen, S. A. Cummer, and S. A. Tretyakov, *Science advances* **5**, eaau7288 (2019).
 - ²⁸ J. Li, A. Díaz-Rubio, C. Shen, Z. Jia, S. Tretyakov, and S. Cummer, *Physical Review Applied* **11**, 024016 (2019).
 - ²⁹ X. Peng, J. Li, C. Shen, and S. A. Cummer, *Applied Physics Letters* **118**, 061902 (2021).
 - ³⁰ L. Quan and A. Alù, *Physical Review Applied* **11**, 054077 (2019).
 - ³¹ L. Quan and A. Alù, *Physical Review Letters* **123**, 244303 (2019).
 - ³² H.-T. Zhou, W.-X. Fu, Y.-F. Wang, Y.-S. Wang, V. Laude, and C. Zhang, *Materials & Design* **199**, 109414 (2021).
 - ³³ P. Georgi, Q. Wei, B. Sain, C. Schlickriede, Y. Wang, L. Huang, and T. Zentgraf, *Science Advances* **7**, eabf9718 (2021).
 - ³⁴ J. Li, S. Kamin, G. Zheng, F. Neubrech, S. Zhang, and N. Liu, *Science advances* **4**, eaar6768 (2018).
 - ³⁵ Z. Meng, H. Yan, M. Liu, W. Qin, G. M. Genin, and C. Q. Chen, *Advanced Science* **10**, 2370133 (2023).
 - ³⁶ J. Li, A. Song, and S. A. Cummer, *Physical Review Applied* **14**, 044012 (2020).
 - ³⁷ X. Jiang, J. Zhao, S.-l. Liu, B. Liang, X.-y. Zou, J. Yang, C.-W. Qiu, and J.-c. Cheng, *Applied Physics Letters* **108** (2016).
 - ³⁸ C. Shi, M. Dubois, Y. Wang, and X. Zhang, *Proceedings of the National Academy of Sciences* **114**, 7250 (2017).